Channel-controlled Janus membrane fabricated by simultaneous laser ablation and nanoparticles deposition for underwater bubbles manipulation Ⓕ

Yanlei Hu ⑩, Weixin Qiu, Yiyuan Zhang, Yachao Zhang, Chuanzong Li, Jiawen Li ⑩, Sizhu Wu, Wulin Zhu, Dong Wu, and Jiaru Chu

COLLECTIONS

Ⓕ This paper was selected as Featured

View Online   Export Citation   CrossMark

ARTICLES YOU MAY BE INTERESTED IN

Simple non-galvanic flip-chip integration method for hybrid quantum systems
Applied Physics Letters **114**, 173501 (2019); https://doi.org/10.1063/1.5089888

Large photovoltaic response in rare-earth doped $BiFeO_3$ polycrystalline thin films near morphotropic phase boundary composition
Applied Physics Letters **114**, 173901 (2019); https://doi.org/10.1063/1.5090911

Effect of poling temperature on piezoelectric and dielectric properties of $0.7Pb(Mg_{1/3}Nb_{2/3})O_3$-$0.3PbTiO_3$ single crystals under alternating current poling
Applied Physics Letters **114**, 172901 (2019); https://doi.org/10.1063/1.5094362

Channel-controlled Janus membrane fabricated by simultaneous laser ablation and nanoparticles deposition for underwater bubbles manipulation [F]

Yanlei Hu,[1,2] [iD] Weixin Qiu,[1] Yiyuan Zhang,[1] Yachao Zhang,[1] Chuanzong Li,[3] Jiawen Li,[1,a] [iD] Sizhu Wu,[3] Wulin Zhu,[1] Dong Wu,[1,a] and Jiaru Chu[1]

AFFILIATIONS

[1]CAS Key Laboratory of Mechanical Behavior and Design of Materials, Department of Precision Machinery and Precision Instrumentation, University of Science and Technology of China, Hefei 230026, China
[2]Department of Mechanical Engineering and Department of Civil and Environmental Engineering, Massachusetts Institute of Technology, Cambridge, Massachusetts 02139, USA
[3]Department of Mechanical and Electronic Engineering, Hefei University of Technology, Hefei 230009, China

[a]Electronic addresses: jwl@ustc.edu.cn and dongwu@ustc.edu.cn

ABSTRACT

Reliable manipulation of gaseous bubbles in aqueous media has spurred considerable research interest in recent years due to the tremendous potential ranging from water treatment, catalytic reactions to resource exploration and liquid medicine transportation. However, facile and effective manufacture of functional devices for bubble manipulation is still in great demand. Here, a versatile integrated femtosecond laser-assisted ablation and nanoparticles deposition (FLAND) approach is proposed to obtain Janus organic membranes having mesoscale pore arrays for unidirectional transportation of underwater bubbles. Selective silica nanoparticles deposition occurs simultaneously with laser ablation, enabling superaerophilic/superaerophobic Janus membranes without toxic chemical treatment and rigorous bonding. The FLAND method is capable of controlling the wettability of the pore channel, which is revealed to play a crucial role in the bubble penetration behavior. Analogous to an electrical diode, underwater unidirectional penetration of bubbles is demonstrated for gas-related implementations. This fabrication system with an identical femtosecond laser for simultaneous ablation and nanoparticles deposition manifests simplicity and versatility, opening up more possibilities in manufacturing functional surfaces for various applications.

Published under license by AIP Publishing. https://doi.org/10.1063/1.5095615

Underwater manipulation of gaseous bubbles is of significance for industrial, medical, and ocean development purposes.[1–4] For example, prevention of adhesion of gas bubbles on an electrode can significantly promote the electrochemical gas evolution reaction efficiency.[5] Efficient capture or absorption of bubbles can find widespread applications in boosting gas-related reactions[6] and sustained collection of methane gas from the seafloor.[7] Consequently, many efforts have been devoted to manipulating underwater bubbles by using diverse devices, such as chemically treated meshes, superaerophilic cones, and metallic sheets.[8–12] Among them, Janus membranes, consisting of superaerophilic and superaerophobic surfaces on each side, are capable of transporting bubbles unidirectionally and, thus, employed as powerful tools for controllable gaseous bubble manipulation.[8,13,14]

Similar to the preparation of functional surfaces with controlled water wetting properties, the fabrication of devices for bubble manipulation inevitably involves surface energy modification using a complex process or hazardous chemicals, e.g., oxygen plasma or fluorination is generally needed for tailoring the surface energy, which results in a multistep process, low efficiency, and limited function-durability.[15,16] Furthermore, in order to obtain a Janus membrane with two different extreme bubble wettabilities, a meticulous bonding process is needed,[8] leading to increased fabrication complexity and decreased efficiency. Therefore, the development of a stable, efficient, and flexible method for controllable bubble manipulation is still highly desired.

Here, an integrated femtosecond laser-assisted ablation and nanoparticles deposition (FLAND) approach is developed to realize Janus organic membranes having mesoscale pore arrays for underwater unidirectional bubble penetration. The Janus membrane is accomplished by single-step *in-situ* femtosecond laser fabrication without
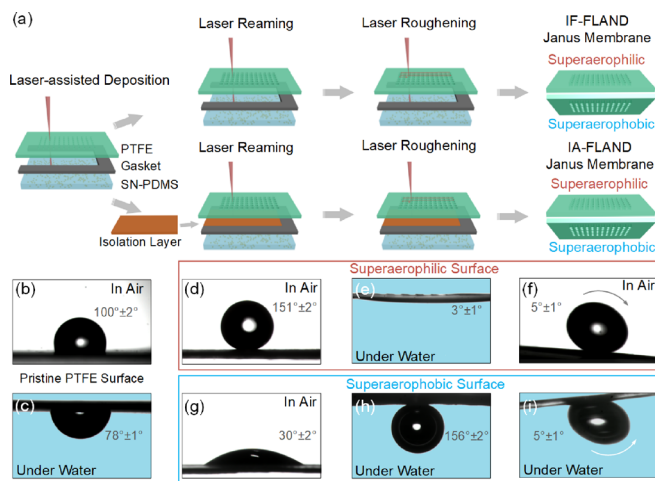
FIG. 1. (a) Schematic of the isolation-free FLAND process (upper) and the isolation-assisted FLAND process (lower). (b) WCA in air and (c) underwater BCA characterization on the flat pristine PTFE surface. Here, the air bubble is generated by a microsyringe pump. The color of water in the image is modified into light blue for clarity (the same hereinafter). (d) and (g) WCA in air, (e) and (h) underwater BCA, and (f) and (i) WSA/underwater BSA characterization of the FLAND-prepared superaerophilic and superaerophobic surfaces, respectively.

multistep chemical treatment and the subsequent bonding process. Silica nanoparticle-embedded Polydimethylsiloxane (SN-PDMS) is used to provide a hydrophilic target material for laser-assisted deposition. One side of Polytetrafluoroethylene (PTFE) exhibits superaerophilicity after laser treatment, while the other side shows superaerophobicity, owing to the selective silica nanoparticles deposition. It is discovered that the wettability of the interior pore wall has a distinct effect on the bubble penetration behavior. At last, an underwater bubble "diode" is demonstrated, which is suitable for gas-related reaction applications.

A multilayer configuration comprising PTFE, a U-shaped polymeric gasket, and SN-PDMS is designed for fabrication, as depicted in Fig. 1(a). The FLAND process consists of three steps, termed as laser-assisted deposition, laser reaming, and laser roughening. First, laser single-point drilling is performed to ablate the membrane and simultaneously induce silica nanoparticles deposition on the lower surface of the PTFE. Second, laser reaming is carried out for machining through holes (300 μm) around the drilling spots. The mesoscale pore array can enhance the flux penetration of underwater bubbles compared to previously reported micro/nanopores[17] or porous materials.[18] Finally, the upper surface of PTFE is further treated by the laser with a relatively low power by raster scanning to further increase surface roughness, enabling the superaerophilic surface. To control the wettability of the interior wall of pores, a cover glass slide is inserted into the gasket as an isolation layer between PTFE and SN-PDMS to prevent deposition of hydrophilic silica nanoparticles onto the interior pore wall during laser reaming. For the sake of convenience, the fabrication process without an isolation layer is termed the "isolation-free" FLAND process (IF-FLAND) and the one with an isolation layer is termed the "isolation-assisted" FLAND process (IA-FLAND) in the following paragraphs.

During the laser drilling process of FLAND, the laser first ablates through PTFE and bombards the SN-PDMS surface, depositing silica nanoparticles on the lower surface of PTFE. Because of the superhydrophilicity of the silica nanoparticles, the lower surface of PTFE becomes hydrophilic after laser ablation and selective nanoparticles deposition. Figures 1(b) and 1(c) show the water contact angle (WCA) in air and the underwater bubble contact angle (BCA) of the pristine PTFE surface, demonstrating that PTFE is hydrophobic (WCA $\sim 100° \pm 2°$). When the surface is immersed in water, a sessile air bubble exhibits a BCA of $78° \pm 1°$. After laser processing, the upper surface of PTFE exhibits superhydrophobicity (WCA $\sim 151° \pm 2°$) [Fig. 1(d)], as well as low surface adhesion with a water sliding angle (WSA) of $5° \pm 1°$ [Fig. 1(f)]. Once immersed in water [Fig. 1(e)], the surface appears to be underwater superaerophilic with a BCA of only $3° \pm 1°$. In contrast, the lower surface of PTFE exhibits hydrophilicity (WCA $\sim 30° \pm 2°$), underwater superaerophobicity (BCA $\sim 156° \pm 2°$), and ultralow bubble adhesion with an underwater bubble sliding angle (BSA) of $5° \pm 1°$ [Figs. 1(g)–1(i)]. It is worth mentioning that the wettability is the same no matter how the Janus membrane is obtained (i.e., via IF-FLAND or IA-FLAND), except that the underwater bubble can penetrate the membrane if the IA-FLAND prepared superaerophobic surface is faced downwards, which will be discussed below.

From the above experimental observation, we can see that the superhydrophobic surface exhibits underwater superaerophilicity, whereas the hydrophilic surface shows underwater superaerophobicity. It is known that the WCA is determined by the surface tension of the three-phase interfaces between solid, liquid, and vapor, which can be deduced from Young's equation, i.e., $\cos\theta_W = (\gamma_{SV} - \gamma_{SL})/\gamma_{LV}$, where γ_{SV}, γ_{SL}, and γ_{LV} are the interfacial energies between the solid-vapor, solid-liquid, and liquid-vapor interfaces, respectively. Similarly, when a gaseous bubble is released onto the surface in an aqueous solution [Fig. 2(a)], a new three-phase interface is formed: $\cos\theta_B = (\gamma_{SL} - \gamma_{SV})/\gamma_{LV}$. Therefore, bubble wettability on a flat solid surface in aqueous media can be considered as the complementary situation of liquid droplet wettability in air: $\theta_B = 180° - \theta_W$. In Figs. 1(b) and 1(c), the WCA of pristine PTFE is $100° \pm 2°$ and the underwater BCA is $78° \pm 1°$, agreeing well with the corollary.

The formation of the Janus membrane is attributed to the single-side deposition of hydrophilic silica nanoparticles on PTFE. In order to verify the effective single-side deposition of silica, the XPS measurement is performed on both sides of the Janus membrane. In comparison with the superaerophilic surface, survey scan of the superaerophobic surface highlights the increase in silicon, oxygen, and carbon contents [Fig. 2(b)]. The Si 2p peak [Fig. 2(c)] is located at the binding energy of 103.3 eV (consistent with O–Si–O bonds in silica), evidently validating that SiO_2 is coated on the superaerophobic surface. The O 1s peak at 532.7 eV is deconvoluted [Fig. 2(d)], ascribed to O-Si-O bonds in silica and Si-O-Si bonds in PDMS. From the high-resolution spectra of C 1s [Fig. 2(e)], it can be clearly deduced that a certain amount of PDMS matrix is deposited together with SiO_2 on the lower surface as an additional peak associated with the typical C-Si bonds in the PDMS polymeric chain appears. There is almost no silicon and oxygen composition on the superaerophilic surface, indicating that no redundant material reaches the upper PTFE surface during laser-assisted deposition.

The morphology of the both sides of the Janus membrane prepared via IF-FLAND is shown in Figs. 3(a)–3(d). It can be seen that the superaerophilic surface is covered with micro/nanoscale hierarchical structures, endowing it with high roughness. The hierarchical
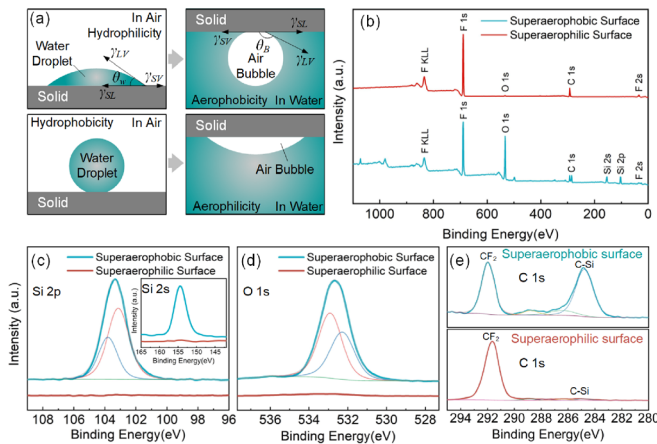
FIG. 2. (a) Relationship between the water wettability in air and the bubble in water on the same solid surface. (b) XPS spectra of the superaerophobic and superaerophilic surfaces of the Janus membrane prepared by FLAND. High-resolution deconvoluted XPS spectra of (c) Si 2p, (d) O 1s, and (e) C 1s on both sides of the FLAND Janus membrane. Inset of (c): XPS spectra for Si 2s.

structure is created by laser raster scanning, giving rise to superhydrophobicity of the PTFE surface. In comparison, the superaerophobic surface is obviously smooth because no laser scanning is applied on the lower side. Flocculent nanostructures are formed by laser-assisted deposition and random accumulation of the target material.

In order to test the underwater bubble behavior of the as-prepared Janus membrane, the superaerophilic surface is placed facing down in water and air bubbles are released from below. As shown in Fig. 3(e), when bubbles float to the superhydrophobic surface, they spread horizontally on the surface. Because the superhydrophobic surface cannot be wetted by water, a thin layer of air film is captured when it is immersed in water.[10,14] As shown in Fig. 3(f), when the bubble comes into contact with the trapped air film, the gas in the bubble rapidly coalesces with the air layer and spreads horizontally. When the membrane is reversed and the superaerophobic surface is faced downwards, the bubbles remain on the superaerophobic surface maintaining a spherical shape, as shown in Figs. 3(g) and 3(h). Water can completely wet the superaerophobic surface and enter the gaps of the hierarchical structures. The bubble is repelled by the water layer due to the repulsive interaction between the liquid and vapor phases. In the process of laser reaming of the mesoscale pores, the inner side of the pore is also sputtered with silica nanoparticles together with the PTFE lower surface due to bombardment of the target SN-PDMS, leading to the hydrophilic channel as depicted in Figs. 3(i) and 3(j). Therefore, water can wet the pore easily and a water column is trapped in the channel when the air bubble comes into contact with the lower surface. The water column can prevent the air bubble from passing to the upper side. To verify this hypothesis, Energy-Dispersive Spectroscopy (EDS) is performed on the interior wall of the mesoscale pore for elemental mapping. As shown in Figs. 3(k) and 3(l), silicon exists on the inner pore side as well as fluorine from PTFE, validating the SiO_2 deposition on the interior pore wall.

If the air bubble wants to penetrate the Janus membrane, the buoyancy of the bubble must overcome the resistance caused by the

water column [Fig. 3(m)]. Figure 3(n) illustrates the forces acting on the water column, including capillary force(surface tension force) F_C, gravity force F_G, hysteresis resistance force F_H, and differential pressure from the upper air pocket and lower air bubble F_P. Capillary force F_C and gravity force F_G can be expressed as follows:

$$F_c = 2\pi r\gamma \cos\theta_W, \qquad (1)$$

$$F_G = \pi r^2 \rho g h, \qquad (2)$$

where r is the radius of the pore, γ is the surface tension of water, θ_W is the WCA in air, ρ is the density of water, and h is the thickness of the Janus membrane. In the quasi-static condition, the differential pressure difference F_P is known to equal the gravity force F_G and the capillary forces F_C from the opposite directions cancel out, owing to the identical three-phase interfacial situation on the top and bottom of the water column. However, when the differential pressure F_P driven by the bubble buoyancy tends to push the water column, the hysteresis resistance force arises to impede the movement of the water column and thus resist the passage of air bubbles[19]

$$F_H = 2\pi r\gamma(\cos\theta_r - \cos\theta_a), \qquad (3)$$

where θ_r and θ_a are the receding and advancing contact angles, respectively. The surface tension of water $\gamma = 7.2 \times 10^{-2}$ N/m. For a hydrophilic surface, water has strong adhesion to the solid surface due to a large contact angle hysteresis, making it difficult to derive the exact value of θ_r and θ_a. Yet, it is reasonable to infer that the hysteresis resistance force is on the order of $2\pi r\gamma \sim 6.8 \times 10^{-5}$ N because the term in the brackets above is not more than two.

From the above discussion, we know that the wettability of the inner side of the pore plays a crucial role in the air bubble behavior. It is reasonable to deduce that the Janus membrane with hydrophobic pores can show dramatically different bubble penetration properties. Consequently, the Janus membrane with hydrophobic channels via the IA-FLAND approach is fabricated. The SEM images of both the sides of the Janus membrane are shown in Figs. 4(a)–4(d). There is no obvious difference in the morphology of that obtained by IF-FLAND, indicating that the addition of the isolation layer does not affect the morphology of the laser treated surfaces. To verify that SiO_2 nanoparticles are not deposited on the inner pore surface, cross-sectional SEM and EDS measurements are carried out in the same manner as the previous section [Figs. 4(e)–4(h)]. It is validated that no SiO_2 is deposited inside the channel because very rare silicon can be found in the elemental mapping. Hence, the channel is hydrophobic and cannot be wetted by water because PTFE has inherent hydrophobicity.

When the Janus membrane is immersed in water with the superaerophilic surface facing down [Figs. 4(i) and 4(j)], the air bubble released underneath the membrane behaves in the same fashion as that in Fig. 3(e). However, when we invert the Janus membrane to let the superaerophilic surface facing downward, the air bubble can penetrate the membrane with ease and spreads out on the upper side [Fig. 4(k)]. When the gas accumulates to a certain amount, it can break away from the upper surface under the action of the buoyancy. The IA-FLAND Janus membrane shows unidirectional transportation of air bubbles analogous to an electrical diode. In Fig. 4(l), we show that the hydrophobic channel between the superaerophobic surface and the superaerophilic surface facilitates the passage of the air bubble. Because the channel cannot be wetted by water, the air pocket is
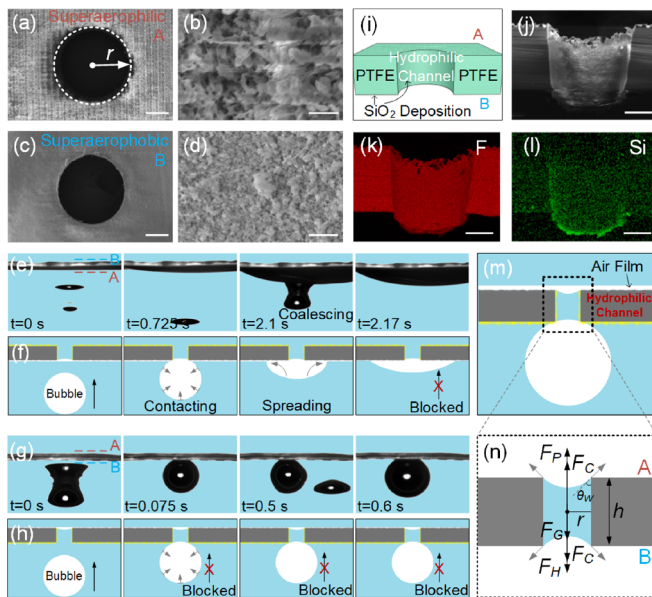
FIG. 3. (a) SEM image of the superaerophilic surface and (c) the superaerophobic surface of the membrane obtained by the IF-FLAND process. The radius of the mesoscale pore r is 150 μm, and the membrane thickness is 300 μm. Scale bars: 100 μm. (b) and (d) show the magnified SEM images corresponding to (a) and (b), respectively. Scale bars: 4 μm. (e) and (f) Release of air bubbles under the superaerophilic surface and horizontal spreading of the bubbles. (g) and (h) Release of air bubbles under the superaerophobic surface and trap of the bubbles. (i) Sketch of the cross section of the Janus membrane that features a hydrophilic channel. (j) SEM image and EDS elemental mappings for (k) F and (l) Si of the cross section of the channel. Scale bars: 100 μm. (m) Illustration of the bubble in contact with the IF-FLAND Janus membrane with the superaerophobic surface facing downwards. (n) Schematic sketch of the forces acting on the water column inside the hydrophilic channel. A denotes the superaerophilic surface, and B denotes the superaerophobic surface.

FIG. 4. (a) SEM image of the superaerophilic surface and (c) the superaerophobic surface of the membrane obtained by the IA-FLAND process. Scale bars: 100 μm. (b) and (d) show the magnified SEM images corresponding to (a) and (b), respectively. Scale bars: 4 μm. (e) Schematic diagram of the cross section of the Janus membrane that features a hydrophobic channel. (f) SEM image and EDS elemental mapping for (g) F and (h) Si of the cross section of the channel. Scale bars: 100 μm. (i) and (j) Release of air bubbles under the superaerophilic surface and horizontal spreading of the bubbles. (k) and (l) Release of air bubbles under the superaerophobic surface and penetration of the bubbles. (m) Phase diagram of the bubble behavior on Janus membranes with different thicknesses and different orientations. (n) Schematic diagram of the forces acting on the bubble to squeeze it through the hydrophobic channel.

trapped in the channel when the Janus membrane is placed in water. When the air bubble comes into contact with the pore from the bottom as explicated in Fig. 4(n), a gas channel forms to connect the bubble and the air film near the upper superaerophilic surface. The gas in the bubble is driven upwards due to the differential Laplace pressure P_L in the gas phase. P_L can be expressed by the Young-Laplace equation:[8] $P_L \sim \gamma \left(\frac{1}{R_1} - \frac{1}{R_2} \right)$, where R_1 and R_2 are the radii of curvature of the air bubble and the air film on the upper superaerophilic surface, respectively. In the initial state, R_2 approaches infinity. R_1 is about 850 μm. The differential Laplace pressure is on the order of 10^2 Pa. As the gas penetrates, the bubble becomes smaller and R_1 decreases rapidly, resulting in larger differential Laplace pressure to further accelerate the bubble passage.

The influence of the membrane thickness on the bubble behavior is also studied. As shown in Fig. 4(m), the air bubble cannot penetrate from the superaerophilic surface to the superaerophobic surface (from A to B), regardless of the membrane thickness and processing method. The air bubble is able to penetrate from the superaerophobic surface to the superaerophilic surface (from B to A) of the IA-FLAND Janus membrane for all the thickness, revealing good bubble diode performance. It is interesting that the air bubble can permeate from the superaerophobic surface to the superaerophilic surface (from B to A)
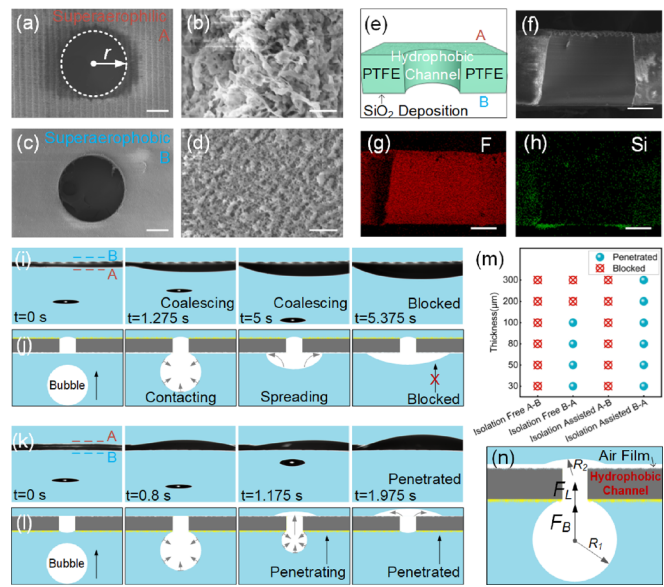
of the IF-FLAND Janus membrane with a relatively slow speed when the thickness is less than 200 μm. According to the force analysis in Fig. 3(n), if the membrane thickness is small enough, the buoyancy of the bubble is possible to overcome the gravity and hysteresis resistance force of the water column trapped in the hydrophilic channel and squeeze it out. Once the water is removed from the pore, a gas channel is generated and the bubble can pass through the membrane driven by differential Laplace pressure.

A proof-of-concept demonstration is provided to show the bubble-manipulation ability of the as-prepared Janus bubble diode. The IA-FLAND Janus membrane is sandwiched between the ends of two empty cylinders and tightened to create an underwater bubble diode device [Fig. 5(a)]. There are two ports of the device close to the superaerophilic surface (A) and the superaerophobic surface (B), respectively. Bromothymol blue solution is used to visually examine the gas permeability, which can change colors with PH values of the solution. Carbon dioxide is introduced into the device from the gas inlet. As we can see from Fig. 5(b) (Multimedia view), when we install the bubble diode device with the superaerophilic surface facing the inlet (i.e., A → B), no color change occurs in the bromothymol blue solution. By inverting the bubble diode device with the superaerophobic surface facing the inlet (i.e., B → A), the color of bromothymol blue solution is found to change gradually from dark blue to maroon [Fig. 5(c) (Multimedia view)], revealing robust unidirectional
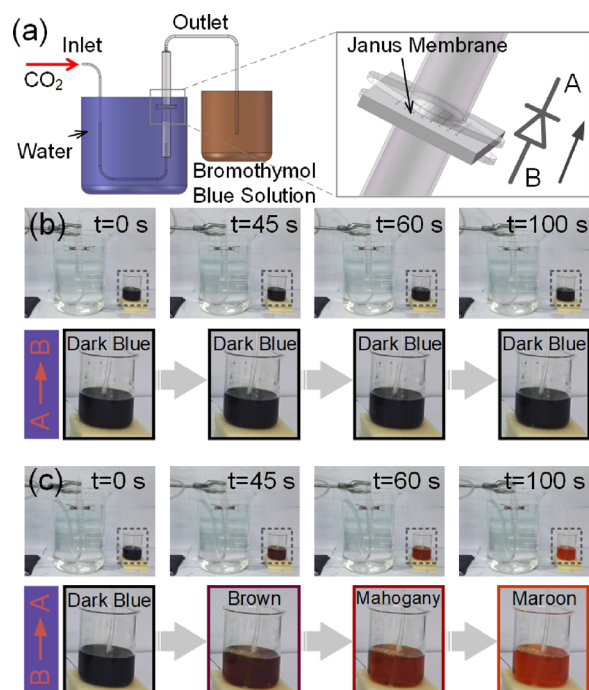
FIG. 5. (a) Layout of the experimental setup for bubble manipulation. (b) Bubbles cannot pass from the superaerophilic surface to the superaerophobic surface (from A to B). The color of bromothymol blue solution remains unchanged. (c) Bubble can penetrate from the superaerophobic surface to the superaerophilic surface (from B to A). The color of bromothymol blue solution changes gradually due to the continuous injection of CO_2. Multimedia views: https://doi.org/10.1063/1.5095615.1; https://doi.org/10.1063/1.5095615.2

transportation ability of the Janus membrane. Comparatively, the color of bromothymol blue solution does not change no matter how the IF-FLAND Janus membrane is installed. The unidirectional transportation ability of the Janus membrane may promote the development of advanced materials for applications in ocean vessels, pipe transportation, and foaming processes.

In summary, superaerophilic/superaerophobic Janus PTFE membranes with mesoscale pores are fabricated by a versatile femtosecond laser-assisted ablation and nanoparticles deposition method. It is revealed that the wettability of the interior wall of the pore channel plays a crucial role in the bubble permeability. This finding is of great significance to deepen insight into the roles of the wettability gradient in controlling bubble penetration for exploring more gas-involved applications. Furthermore, functional devices capable of performing unidirectional bubble transportation analogous to the electrical diode are demonstrated, holding great potential for a wide range of applications including water treatment and medical devices.

REFERENCES

[1]Z. Lu, W. Zhu, X. Yu, H. Zhang, Y. Li, X. Sun, X. Wang, H. Wang, J. Wang, and J. Luo, Adv. Mater. **26**(17), 2683–2687 (2014).

[2]T. A. Ternes, M. Meisenheimer, D. McDowell, F. Sacher, H.-J. Brauch, B. Haist-Gulde, G. Preuss, U. Wilme, and N. Zulei-Seibert, Environ. Sci. Technol. **36**(17), 3855–3863 (2002).

[3]S. Mazloomi and N. Sulaiman, Renewable Sustainable Energy Rev. **16**(6), 4257–4263 (2012).

[4]C. Zhang, M. Cao, H. Ma, C. Yu, K. Li, C. Yu, and L. Jiang, Adv. Funct. Mater. **27**(43), 1702020 (2017).

[5]M. S. Faber, R. Dziedzic, M. A. Lukowski, N. S. Kaiser, Q. Ding, and S. Jin, J. Am. Chem. Soc. **136**(28), 10053–10061 (2014).

[6]P. Wang, T. Hayashi, Q. A. Meng, Q. Wang, H. Liu, K. Hashimoto, and L. Jiang, Small **13**(4), 1601250 (2017).

[7]M. Kondo, T. Okubo, A. Asami, S. i Noro, T. Yoshitomi, S. Kitagawa, T. Ishii, H. Matsuzaka, and K. Seki, Angew. Chem. Int. Ed. **38**(1–2), 140–143 (1999).

[8]C. Pei, Y. Peng, Y. Zhang, D. Tian, K. Liu, and L. Jiang, ACS Nano **12**, 5489–5494 (2018).

[9]C. Yu, M. Cao, Z. Dong, J. Wang, K. Li, and L. Jiang, Adv. Funct. Mater. **26**(19), 3236–3243 (2016).

[10]C. Yu, P. Zhang, J. Wang, and L. Jiang, Adv. Mater. **29**(45), 1703053 (2017).

[11]C. Huang and Z. Guo, Nanoscale **10**(42), 19659–19672 (2018).

[12]J.-A. Duan, X. Dong, K. Yin, S. Yang, and D. Chu, Appl. Phys. Lett. **113**(20), 203704 (2018).

[13]H. C. Yang, J. Hou, L. S. Wan, V. Chen, and Z. K. Xu, Adv. Mater. Interfaces **3**(9), 1500774 (2016).

[14]J. Chen, Y. Liu, D. Guo, M. Cao, and L. Jiang, Chem. Commun. **51**(59), 11872–11875 (2015).

[15]J. Yong, F. Chen, J. Huo, Y. Fang, Q. Yang, J. Zhang, and X. Hou, Nanoscale **10**(8), 3688–3696 (2018).

[16]S. Yan, F. Ren, C. Li, Y. Jiao, C. Wang, S. Wu, S. Wei, Y. Hu, J. Li, and Y. Xiao, Appl. Phys. Lett. **113**(26), 261602 (2018).

[17]M. H. Ibrahim, M. H. El-Naas, Z. Zhang, and B. Van der Bruggen, Energy Fuels **32**(2), 963–978 (2018).

[18]Y. Zhao, H. Wang, H. Zhou, and T. Lin, Small **13**(4), 1601070 (2017).

[19]E. B. Dussan V, and R. T.-P. Chow, J. Fluid Mech. **137**, 1–29 (1983).